

1 **Temporal changes in rainfall intensity-duration thresholds for post-** 2 **wildfire flash floods in Southern California**

3 Tao Liu^{1,2}, Luke A. McGuire¹, Nina Oakley³, Forest Cannon³

4 ¹Department of Geosciences, University of Arizona, Tucson, AZ 85721-0011, USA

5 ²Department of Hydrology and Atmospheric Sciences, University of Arizona, Tucson, AZ 85721-0011, USA

6 ³Center for Western Weather and Water Extremes, Scripps Institution of Oceanography, University of California, San Diego,
7 La Jolla, CA, USA

8 *Correspondence to:* Tao Liu (liutao@arizona.edu)

9 **Abstract.** Rainfall intensity-duration (ID) thresholds are commonly used to assess flash flood potential downstream of burned
10 watersheds. High-intensity and/or long-duration rainfall is required to generate flash floods as landscapes recover from fire,
11 but there is little guidance on how thresholds change as a function of time since burning. Here, we force a hydrologic model
12 with radar-derived precipitation to estimate ID thresholds for post-fire flash floods in a 41.5 km² watershed in southern
13 California, USA. Prior work in this study area constrains temporal changes in hydrologic model parameters, allowing us to
14 estimate temporal changes in ID thresholds. Results indicate that ID thresholds increase by more than a factor of 2 from post-
15 fire year 1 to post-fire year 5. Thresholds based on averaging rainfall intensity over durations of 15-60 minutes perform better
16 than those that average rainfall intensity over shorter time intervals. Moreover, thresholds based on the 75th percentile of radar-
17 derived rainfall intensity over the watershed perform better than thresholds based on the 25th or 50th percentile of rainfall
18 intensity. Results demonstrate how hydrologic models can be used to estimate changes in ID thresholds following disturbance
19 and provide guidance on the rainfall metrics that are best suited for predicting post-fire flash floods.

20

21 **1 Introduction**

22 Heightened hydrologic responses are common within and downstream of recently burned areas, resulting in an increased
23 likelihood of flash floods. Rainfall intensity-duration (ID) thresholds are commonly used to assess the potential for flash floods
24 (Moody and Martin, 2001; Cannon et al., 2008). Many past studies aimed at defining thresholds for flash floods focus on the
25 first 1-2 years following fire (Cannon et al., 2008; Wilson et al., 2018). Since the hydrologic impacts of fire are transient,
26 rainfall ID thresholds associated with flash floods are likely to change as a watershed recovers (Ebel and Martin, 2017; Ebel
27 and Moody, 2017; Moreno et al., 2019; Ebel, 2020). It may take more than a decade for hydrologic responses to return to pre-
28 fire levels, yet there is limited guidance on how the magnitude and utility of rainfall ID thresholds change with time since
29 burning. Given the increased frequency and size of fire in many geographic and ecological zones (e.g. Gillett et al., 2004;
30 Westerling et al., 2006; Kitzberger et al., 2017), it is of growing importance to quantify the best metrics for assessing flash-
31 flood potential in the immediate aftermath of fire as well as how these metrics change throughout the recovery process (e.g.
32 Ebel, 2020).

33
34 Rainfall ID thresholds for flash floods are typically defined using historic data that relates rainfall over different intensities
35 and durations to an observed hydrologic response, namely the presence or absence of flooding (e.g. Cannon et al., 2008). Due
36 to the stochastic nature of rainfall over burned areas and limited observations throughout the recovery process, there is a
37 paucity of data that can be used to derive empirical thresholds for flash flooding beyond one year of recovery. Hazards
38 associated with flash flooding, however, may exist downstream of burned areas well beyond one year of recovery. Wildfire
39 alters rainfall-runoff partitioning and flood routing by incinerating vegetation and reducing interception capacity (Stoof et al.,
40 2012, Saksa et al., 2020), decreasing hydraulic roughness, and reducing soil infiltration capacity (Larsen et al., 2009, Ebel and
41 Moody, 2013). Reductions in infiltration capacity are often attributed to fire-induced soil water repellency (Ebel and Moody,
42 2013), which is generally strongest immediately following a fire and then decays over time scales ranging from one year to
43 more than five years (Dyrness, 1976; Huffman et al., 2001; Larsen et al., 2009), though surface soil sealing (Larsen et al.,
44 2009) and hyper-dry conditions (Moody and Ebel, 2012) are also known to play important roles. Vegetation recovery, which
45 may influence temporal changes in hydraulic roughness and canopy interception, can take five years or longer. Cannon et al.
46 (2008) collected sufficient data over a two-year time period following fire in southern California, USA, to define separate
47 rainfall ID thresholds for post-fire debris flows and flash floods in the first- and second-years following fire. They found that
48 the ID thresholds for flash floods and debris flows may increase by as much as 25 mm/h after one year of recovery, a change
49 that they attributed to a combination of vegetation growth and sediment removal as a result of rainstorms during the first post-
50 fire year.

51
52 Rainfall ID thresholds are often defined over a range of durations, though averaging rainfall intensity over a particular duration
53 may provide a more reliable threshold. Post-fire hydrological response in the first few years is often best related to rainfall

54 intensity over short durations (less than 60 min) (Staley et al., 2017; Moody and Martin, 2001). In their efforts to define rainfall
55 ID thresholds for post-fire debris flows, Staley et al. (2013) showed that averaging rainfall intensities over durations between
56 15 minutes and 60 minutes resulted in thresholds that performed better relative to those associated with longer durations. One
57 potential explanation for this observation is that post-fire debris flows are often triggered by runoff in steep, low-order
58 drainages, which both Kean et al. (2011) and Raymond et al. (2020) have found to be highly correlated with rainfall intensities
59 averaged over similarly short time intervals (10-15 minutes). Moody and Martin (2001) have also documented a substantial
60 increase in peak discharge following wildfire once the 30-minute rainfall intensity (I_{30}) crossed a threshold value, suggesting
61 that I_{30} may be a consistent predictor of flash flood activity in recently burned watersheds. Moody and Martin (2001) suggest
62 that peak I_{30} can be used to set the threshold for early-warning flood systems. The optimal duration for defining post-fire flash
63 floods thresholds, as well as how it may change with time, remains relatively unexplored.

64
65 Rain gage records are typically used to derive rainfall ID thresholds for flash flood and post-fires debris flows (Staley et al.,
66 2013; Staley et al., 2017). Post-fire debris flows, however, tend to initiate in small ($<1 \text{ km}^2$), steep watersheds. In these small
67 watersheds, the rainfall intensity responsible for initiating a debris flow can be characterized by a single rain gage installed
68 near the initiation zone. Flash floods differ in that they tend to occur at larger spatial scales where rainfall is spatially variable
69 and may not be adequately characterized by data from a single rain gage. Radar-derived precipitation estimates, which can
70 provide high spatiotemporal resolution of rainfall intensity, present opportunities to develop basin-specific thresholds for post-
71 fire flash floods. However, high spatiotemporal variability in rainfall intensity also brings new challenges when employing
72 radar-derived precipitation in flood warning practice. In particular, what is the best way to summarize spatially and temporally
73 variable rainfall intensity information with a single metric that can be used as a threshold? How does hydrological recovery
74 following fire influence the generation of flash floods and the metrics that are best suited for their prediction? Data-driven
75 approaches to answering these and related questions may be hampered by limited monitoring of post-fire hydrologic response
76 throughout the recovery period and the stochastic occurrence of rainfall over burned areas, which limits opportunities for
77 observations. Given a well-constrained hydrologic model that accounts for changes associated with post-fire recovery, it is
78 possible to use numerical experiments to understand relationships between time since burning, the spatiotemporal patterns of
79 rainfall over a watershed, and the occurrence of flash floods.

80
81 Here, we use observed patterns of spatially and temporally varying radar-derived rainfall estimates over a 41.5 km^2 watershed
82 in the San Gabriel Mountains of southern California, USA, to (1) determine the optimal method to define a rainfall ID threshold
83 for flash floods, and (2) identify changes in rainfall ID thresholds for flash floods as a function of time since burning. The
84 watershed, which we refer to as the upper Arroyo Seco, burned during the 2009 Station Fire (USDA Forest Service, 2009).
85 Liu et al. (2021) used rain and stream gage data collected at different times following the fire to calibrate the KINEROS2
86 hydrologic model for this watershed, enabling them to quantify temporal changes in model parameters as a function of time
87 since burning. Combining this calibrated model with spatially explicit, radar-derived estimates of rainfall intensity during 34

88 rainstorms, we explore the utility of different rainfall ID metrics as flash flood thresholds and quantify temporal changes in
89 those thresholds through the first five years of recovery. Results provide insight into the magnitude of temporal changes in
90 flash flood thresholds in the densely populated, fire-prone region of southern California. Findings also provide guidance for
91 the magnitude of change expected in rainfall ID thresholds for flash floods during the post-fire recovery period in chaparral-
92 dominated environments similar to southern California. More generally, results support the development of early warning
93 systems for flash floods by identifying specific metrics that can be computed using spatially variable rainfall intensity estimates
94 to assess the potential for flash flooding. The optimal rainfall ID metrics identified in this study could be helpful when issuing
95 flash flood warnings based on radar-derived precipitation estimates or data from several real-time rain gages within a
96 watershed.

97 2 Study Area

98 **Figure 1: Modified from figure 1 in Liu et al. (2021) (a) The location of the upper Arroyo Seco watershed within California. The red**
99 **triangle indicates the location of the USGS stream gage (11098000); (b) Shaded relief showing the study watershed with the USGS**
100 **stream gage (red triangle; 34°13 20", -118°10 36"); (c) Soil burn severity for the 2009 Station fire. Burn severity percentages are for**
101 **planform area within each category.**

102
103 The upper Arroyo Seco watershed drains the 41.5 km² area above USGS stream gage station (11098000) near Pasadena in the
104 San Gabriel Mountains (Figure 1). The upper Arroyo Seco was burned in the August-October 2009 Station Fire, which burned
105 more than 80% of the watershed at moderate to high soil burn severity (USDA Forest Service, 2009). Dominant shrubs and
106 chaparral, such as chamise (*Adenostoma fasciculatum*) and manzanita (*Arctostaphylos spp.*), were completely consumed with
107 severe soil heating in isolated patches throughout many areas burned at moderate to high severity (USDA Forest Service,
108 2009). Soils in this area are typically sand and silty-sand textured and thin (<1 m) with partial exposure of bedrock (Staley et
109 al., 2014). The majority of rainfall in the study area typically occurs in the cool season, between December and March, while
110 warm, dry conditions dominate from April to early November. The San Gabriel Mountains also experience some of the most
111 frequent short-duration, high-intensity rainfall in the state (Oakley et al., 2018a).

112
113 Due to wildfire-induced changes in surface conditions, including canopy cover and soil-hydraulic properties, runoff generation
114 in the first year following the fire was likely dominated by infiltration excess overland flow (Schmidt et al., 2011, Liu et al.,
115 2021). Enhanced soil water repellency (SWR), which helps promote low infiltration capacity, and extensive dry ravel, which
116 loads channels with fine-grained hillslope sediment, are both commonly observed after fires in the San Gabriel Mountains
117 (e.g., Watson and Letey, 1970; Hubbert and Oriol, 2005; Lamb et al., 2011; Hubbert et al., 2012). Rengers et al. (2019)
118 calibrated a hydrologic model using data from small watersheds (0.01-2 km²) burned by the Station Fire and found relatively
119 low values for saturated hydraulic conductivity (K_s), generally between 2-10 mm/h. These results are consistent with values

120 for saturated hydraulic conductivity inferred by Liu et al. (2021) via model calibration in the upper Arroyo Seco watershed.
121 The impact of dry ravel, which reduces grain roughness in the channel network, and reduced vegetation density led to estimates
122 of Manning s_n in the channels of the upper Arroyo Seco of approximately $0.09 \text{ s m}^{-1/3}$ in the first year following fire (Liu et
123 al., 2021). These hydrologic changes led to widespread flooding and debris flows during multiple rainstorms in the first winter
124 after the fire (Kean et al., 2011; Oakley et al., 2017). As hydrologic recovery began over the next several years, the watershed-
125 scale K_s and Manning s_n generally increased and likely started to mitigate the flash flood risk (Liu et al., 2021).

126 **3 Data and Methods**

127 **3.1 Radar-derived precipitation**

128 Weather radar coverage is adequate for estimating rainfall over the study area (NOAA 2021), and radars have been operational
129 since the mid-1990s. This allows us to utilize observed data to capture temporal and spatial characteristics of storms impacting
130 the study area, a region of complex terrain. We sought to identify storms in the study area that produced moderate-to-high
131 intensity rainfall to use as inputs to a hydrologic model to simulate flood responses. Storm events were selected within the
132 period for which observations are archived for the two operational NWS Next-Generation Weather Radar installations
133 (NEXRAD; NOAA 1991) that cover the study area, KSOX, (Santa Ana), and KVTX (Ventura). Archives for the radars begin
134 in 1997 and 1995, respectively.

135
136 We compiled storm events starting with those known to have produced high intensity rainfall and a debris flow response in
137 the San Gabriel Mountains (e.g., Table 1 in Oakley et al., 2017) as well as other storms that produced high-intensity rainfall
138 in the region (e.g., Oakley et al., 2018b, Cannon et al., 2018). We then used hourly rainfall observations from the Clear Creek
139 (2002-present), San Rafael Hills (2005-present), and Heninger Flats (2010-present) Remote Automated Weather Stations
140 (RAWS, acquired from raws.dri.edu) as indicator gages for the study area. This further limited us to post-2002 events outside
141 of the literature. All gages are <10 km from the watershed of interest; there were no long-record gages within the watershed.
142 We used 15 mm/h as a threshold for moderate to high intensity rainfall and extracted all events from the gage record meeting
143 or exceeding this value to develop a list of events of interest. This threshold generally corresponds with a 1-year average
144 recurrence interval storm event in the study area (NOAA Atlas 14). This value falls between the California-Nevada River
145 Forecast Center's flash flood guidance for unburned areas in the region (~22-25 mm/h; CNRFC 2021) and regional thresholds
146 for post-wildfire debris flows in this region at a point (12.7 mm/h, Cannon et al. 2008; Staley et al. 2013). This threshold
147 allows us to focus on storms that have a high potential to generate floods, while keeping the number of storms to a manageable
148 level for data processing. We reviewed the radar data for these events at which point some of the selected events could not be
149 utilized due to radar outages or poor data quality. This exercise presented us with 34 storm events (Table S1).

150

151 Various atmospheric processes may contribute to generation of moderate-to-high rainfall intensities (e.g., Oakley et al., 2017),
152 resulting in differing spatial and temporal precipitation patterns over a burn area. To ensure the events selected captured
153 variability in spatial and temporal precipitation characteristics, we evaluated the spatial characteristics of the events. We found
154 rainfall patterns could generally be categorized into four main spatial patterns at the scale of several tens of kilometers: (1) a
155 broad pattern, a contiguous area of moderate-to-high intensity precipitation (>45 dBZ) spanning tens of kilometers; (2) a
156 scattered pattern with numerous cells of moderate to high precipitation that are not spatially continuous; (3) an isolated pattern,
157 with one to a few isolated cells of moderate-to-high intensity rainfall separated by non-precipitating areas several to tens of
158 kilometers in extent; (4) a narrow cold frontal rainband (NCFR)—a north-south oriented narrow band (~3-5 km wide, tens to
159 100 km in length) of very high intensity rainfall (e.g., Oakley et al., 2018b; Cannon et al., 2020; Figure S1 in Supplement). At
160 the <10 km horizontal scale (the scale of the watershed), it was harder to identify meaningful patterns and distinctions, though
161 the larger scale signals imply varying spatial and temporal patterns of precipitation as each pass over the watershed. A table
162 of storm events and their characteristics is available in Table S1 in the Supplement.

163
164 An approximate start and end time were determined for each event using the Clear Creek RAWS gauge as an indicator. Start
165 time was determined by identifying the time of maximum 1h rainfall in the event and going back in time to the first of three
166 consecutive hours of >1.5 mm/h precipitation. The end of an event was determined as the last hour where precipitation dropped
167 below 3 mm/h for at least two consecutive hours.

168
169 Level-II base reflectivity (<https://www.ncdc.noaa.gov/wct/>) between the start and end time of each event was downloaded
170 from both the KSOX and KVTX radars. The data were used to generate spatially-distributed precipitation over the study area.
171 Radar imagery concurrent with the gauge-based record of high intensity rainfall events was converted to a composite maximum
172 reflectivity product at 250 m spatial and 5-minute temporal resolution. Conversion of radar reflectivity to rain rate required
173 the application of an empirically derived reflectivity (Z) to rain rate (R) relationship (e.g. Marshall and Palmer 1948). The Z-
174 R relationship is conventionally represented by the equation $Z = aR^b$, which includes parameters a and b to account for
175 variations in precipitation for a given reflectivity arising from differences in the drop size distribution. Due to the lack of
176 previous studies investigating Z-R relationships in precipitating conditions over the region of interest, there are no standard a
177 and b parameters to apply to the reflectivity data analyzed here. Thus, five well-known and previously published Z-R
178 relationships were applied to the gridded reflectivity values. Supplement S3 lists the different Z-R relationships applied here
179 and the general conditions for which they are suitable. Although the Z-R relationships used here are not based on observations
180 from the present study's region of interest, the variation of a and b parameters yields an estimate of precipitation uncertainty.
181 It is worth noting that a number of additional sources of radar measurement uncertainty exist that are not evaluated in depth
182 here, including beam broadening, topographic blocking and scan elevation. However, this was not of primary concern since
183 the goal of this study was to generate realistic spatial and temporal patterns of rainfall over the watershed with varying intensity

184 that could be used to force the KINEROS2 hydrologic model. The goal was not to reproduce the observed hydrologic response
185 resulting from a particular set of rainstorms.

186
187 As a range of precipitation intensities for each storm result from the application of the five different Z-R relationships (e.g.,
188 Figure S2 in Supplement), we utilize these as plausible storms of varying precipitation intensity to increase our storm sample
189 size, such that we apply 34 storms * 5 Z-R relations = 170 precipitation scenarios as inputs to KINEROS2. These 170 scenarios
190 were then processed for ingestion into KINEROS2 (Figure 2).

191
192 **Figure 2: Delineation of rainfall intensity-duration threshold for post-fire flash flood**

193 194 3.2 Summary metrics for spatially and temporally varying rainfall

195 In search of a spatiotemporel summary metric that may serve as a reliable flash flood threshold, we begin by describing a
196 methodology to summarize spatially and temporally varying rainfall over a watershed. For a given rainstorm, the rainfall
197 intensity time series at a single point, such as a single radar pixel, can be summarized by computing a moving average of
198 intensity over a specified duration, D . Letting t denote time and R denote the cumulative rainfall (mm), we define the rainfall
199 intensity over a duration D at any given pixel within the watershed as

$$I_D(t) = \frac{R(t) - R(t - D)}{D} \quad (1)$$

200
201 Here, we compute $I_D(t)$ for each pixel for durations of 5, 10, 15, 30, and 60 minutes. Since the intensity in each radar pixel
202 could have a unique value, we also need a way to summarize $I_D(t)$ in space. One option would be to take the median of $I_D(t)$
203 to determine a typical value of I_D within the watershed at each time, t . However, the median may not be a good predictor of
204 flash flooding since one could envision a scenario where it is only raining over 1/3 of the watershed, yet it is raining with
205 sufficient intensity to generate a flash flood. We therefore compute the j^{th} percentile of $I_D(t)$ at each time, t , for j between 1
206 and 99. We denote the j^{th} percentile of $I_D(t)$ as $I_D^j(t)$. For each rainstorm, we focus our analysis on the peak value of $I_D^j(t)$
207 which we denote as I_D^j . As an example, I_{30}^{50} would be computed by defining I_{30} for all radar time steps within a rainstorm,
208 determining the median value of I_{30} over the watershed at each of those time steps, and then taking the maximum of that time
209 series of median I_{30} intensities. This analysis yields 495 different metrics (I_D^j for $j=1,2,\dots,99$ and $D=5,10,15,30,60$) that
210 summarize spatially and temporally varying rainfall intensities over the watershed. In the following sections, we describe how
211 we test the utility of each of these 495 different metrics as a flash flood threshold. A threshold defined by I_D^j would denote a
212 threshold where (100- j)% of the watershed experiences rainfall of duration D with an intensity of I or greater.

213 3.3 Hydrological modeling

214 We used the KINEROS2 (K2) hydrological model to simulate the rainfall partitioning, overland flow generation, and flood
215 routing in the upper Arroyo Seco watershed. K2 is an event-scale, distributed-parameter, process-based watershed model,
216 which has been used extensively for rainfall-runoff processes in semi-arid and arid watersheds (Smith et al., 1995; Goodrich
217 et al., 2012). Liu et al. (2021) used rain gage data in combination with the USGS stream gage installed at the outlet of the
218 upper Arroyo Seco watershed to calibrate K2 during different stages of the post-fire recovery process. We use the same model
219 setup for simulations in this study. In particular, the 41.5 km² watershed was discretized into 1289 hillslope planes and these
220 planes were connected by a stream network of 519 channel segments based on a one-meter LiDAR-derived digital elevation
221 model (DEM). After accounting for a fixed interception depth of 2.97 mm based on land cover look-up table in the Automated
222 Geospatial Watershed Assessment toolkit (AGWA; Miller et al., 2007), infiltration of rainfall into soil is represented using the
223 Parlange et al. (1982) approximation. Overland flow and channel flow are modeled by kinematic wave equations. Both
224 saturated hydraulic conductivity on hillslopes (K_{sh}) and hydraulic roughness in channels (n_c) primarily determine runoff
225 generation and the shape of hydrograph, including total runoff volume, peak discharge rate, time to peak (Canfield et al., 2005;
226 Yatheendradas et al., 2008; Menberu et al., 2019). Other parameters, such as hydraulic roughness (n_h) and capillary drive (G_h)
227 on hillslopes, had a relatively minor impact on modelled runoff after the Station Fire in the upper Arroyo Seco watershed (Liu
228 et al., 2021).

229

230 **Table 1. Summary of model parameters for post-fire year 1, 2, 3, and 5. The saturated hydraulic conductivity on**
231 **hillslopes (K_{sh}) and hydraulic roughness in channels (n_c) are the average of values calibrated in post-fire years 1, 2,**
232 **3, and 5 (Liu et al., 2021)**

233

234 Liu et al. (2021) found that both K_{sh} and n_c were lowest immediately after the fire. K_{sh} increased, on average, by approximately
235 4 mm/h/yr during the first five years of recovery, whereas n_c increased by more than a factor of two after 1 year of recovery
236 and then remained relatively constant. We focus here on simulating the response to rainfall in the first five years following the
237 fire where the watershed is likely most vulnerable to extreme responses. To represent the temporal changes in K_{sh} and n
238 documented by Liu et al. (2021) following the fire, we used different values of K_{sh} and n_c for each post-fire year (i.e. post-fire
239 years 1, 2, 3, and 5) based on the values calibrated by Liu et al. (2021) in post-fire years 1, 2, 3, and 5 (Table. 1). Liu et al.
240 (2021) were unable to calibrate the necessary K2 parameters in post-fire year 4 so we do not perform any simulations to
241 constrain flash flood thresholds in that year. Initial soil moisture is set to a volumetric soil-water content of 0.1, following Liu
242 et al. (2021). Other parameters were also given the same values as the calibrated K2 model, including saturated hydraulic
243 conductivity of channels (1 mm/hr), net capillary drive of channels (5 mm), hydraulic roughness of hillslopes (0.1 s/(m^{1/3})),
244 net capillary drive of hillslopes (50 mm), and soil porosity of 0.4. With this model set-up, we simulate the response to each of
245 the 170 rainstorms for post-fire years 1, 2, 3, and 5.

246

247 3.4 Rainfall intensity-duration thresholds

248 Each K2 simulation results in a modeled hydrograph at the watershed outlet. As a first step towards defining a flash flood
249 threshold, it is necessary to determine, based on the modeled time series of discharge, whether or not a flash flood would have
250 occurred. We defined the flash flood level as the discharge required to exceed bankfull flow (Sweeney, 1992), which we
251 assumed was equal to the two-year flood (Leopold et al., 1964). To determine the discharge associated with the two-year flood,
252 we performed a flood frequency analysis using HEC-SSP v2.2 (Bartles et al., 2019) based on annual maximum records at the
253 USGS stream gage station (11098000). The discharge associated with the two-year flood at the stream gage station is 15.3
254 m³/s, with a 95% confidence interval of 12.3-19.2 m³/s (Figure S3). A flash flood threshold by this definition can be viewed
255 as conservative since it may only indicate the onset of minor flooding as water begins to spill out of the channel. Based on this
256 definition, we then used two approaches to identify the rainfall ID threshold for flash floods (Figure 2).

257
258 The first approach is based on a linear regression analysis that relates peak discharge with different rainfall ID metrics, namely
259 I_D^j for different values of j and D . Using simulations of 170 rainfall-runoff events in each post-fire year, it is possible to
260 determine a relationship for peak discharge (Q) as a function of I_D^j . Then, the rainfall ID threshold can be found by determining
261 the rainfall intensity at which the peak discharge exceeds the bankfull capacity. The simplest quantitative relation is a linear
262 regression:

$$Q = mI_D^j + k \quad (2)$$

263
264 where Q is the peak discharge (m³/s) of a simulated hydrograph at the outlet, I_D^j denotes rainfall intensity (mm/hr) for the
265 rainstorm that produced the hydrograph, and m and k denote the slope and y-intercept of the linear regression, respectively.
266

267 Considering the channel dimensions and resolution of the DEM used in the K2 model, we selected intensity-discharge (I_D^j - Q)
268 pairs associated with Q greater than 2 m³/s. The flow depth associated with Q less than 2 m³/s would be very small and any
269 impact from such flow would be negligible. The parameters in the linear equation (1) with the maximum determination
270 coefficient (R^2_{\max}) were estimated using least-squares linear regression in the SciPy Python library for the selected I_D^j - Q pairs.

271 A total of 495 linear regressions were produced for each year because I_D^j can take on 495 different values (5 durations, 99
272 percentiles) for each rainstorm. For each post-fire year, we then identified the maximum R^2 value for each duration as a
273 function of percentile from 1st to 99th (Figure 3). The rainfall ID threshold for flash flooding in each year was found, for each
274 duration, from the linear relation associated with the largest R^2 (Figure 4).
275

276 **Figure 3: The determination coefficient (R^2) and 95% confidence interval associated with the linear regression between**
277 **I_D^j and peak discharge in post-fire year 1, 2, 3, and 5. Data used to fit the linear relation are from events with peak**
278 **discharge greater than $2 \text{ m}^3/\text{s}$.**

280 **Figure 4: The rainfall intensity-duration threshold for flash flood derived from the best linear relation for different**
281 **durations and percentiles of the most intense rainfall field in post-fire year 1, 2, 3, and 5.**

283 We also estimated the 95% confidence interval (CI) of both R^2 and the rainfall ID threshold by performing bootstrapping
284 resampling on 170 rainfall-runoff events for each year. The number of replications is 50. The 95% CI was constructed with
285 the 2.5 percentile and the 97.5 percentile of the ranked R^2 or rainfall ID threshold.

287 The second approach for determining rainfall ID thresholds is based on a receiver operating characteristic (ROC) analysis
288 following Staley et al. (2013). We assess the utility of a potential threshold (e.g. $I_{30}^{50} = 20 \text{ mm/hr}$), by computing the threat
289 score (TS) associated with using that threshold to define the transition between rainstorms that produce flash floods and those
290 that do not. The TS, as one of the ROC utility functions, measures the fraction of forecast events that were correctly predicted:

$$TS = \frac{TP}{TP + FP + FN} \quad (3)$$

291 where TP, FP, and FN denote a true positive, false positive, and false negative, respectively. Flash flood occurrence (true or
292 false) is determined by comparing the peak discharge of each simulated hydrograph with the flash flood level ($15.3 \text{ m}^3/\text{s}$). A
293 TP represents an event where rainfall rates exceed the threshold (e.g. $I_{30}^{50} = 20 \text{ mm/hr}$), and a flash flood occurred. A FP
294 represents an event where rainfall rates exceed the threshold, but no flash flood occurred. FN events occur when rainfall rates
295 were below the threshold, yet a flash flood occurred. The optimal TS is 1, meaning use of the threshold resulted in no false
296 positives or false negatives.

298
299 For a given rainfall intensity metric (e.g. the peak 75th percentile of I_{30} , I_{30}^{75} , in year 1), we calculated TS for intensities ranging
300 from 0-100 mm/hr at 0.01 mm/hr intervals (Figure 5). We then identified the threshold associated with the maximum TS
301 (TS_{\max}). The intensity associated with TS_{\max} is the optimal threshold for that rainfall metric (Figure 6). We determined the
302 optimal threshold associated with each of the 495 rainfall metrics for each post-fire year (1,2,3, and 5) (Figure 7). We also
303 estimated the 95% CI of TS and rainfall ID threshold for each year by performing bootstrapping resampling with 50
304 replications.

305

306 **Figure 5: Threat score (TS) of the peak 75th percentile of I_{30} in post-fire year 1. (a) Relationship between rainfall**
307 **intensity and TS; (b) Scatter plots of positive (flood, red circle) and negative (no flood, hollow circle) with the rainfall**
308 **intensity associated with the maximum TS.**

309

310 **Figure 6: The threat scores (TS_{max}) associated with flood occurrence and I_D^j in post-fire years 1, 2, 3, and 5. Data used**
311 **to analyze is from events with peak discharge greater than 2 m³/s.**

312

313 **Figure 7: The rainfall intensity threshold for flash flood derived from the maximum of TS for different durations and**
314 **percentiles of the most intensive rainfall field in post-fire years 1, 2, 3, and 5.**

315 **4 Results**

316 **4.1 Optimal summary metrics for defining rainfall ID thresholds**

317 Linear regression analyses suggest that there is a stronger relationship between I_D^j and peak discharge (Q) as j increases, with
318 the exception of a rapid dropoff in R^2 for $j > 95$ (Figure 3). In post-fire year 1, the maximum R^2 increases with duration (D)
319 from a value of 0.72 associated with $I_{0.5}^{95}$, to 0.75 associated with I_{10}^{85} , 0.80 associated with $I_{15}^{72} - I_{15}^{87}$, 0.87 associated with I_{30}^{81} ,
320 to 0.89 associated with I_{60}^{89} . In post-fire years 2-5, the R^2 values associated with durations of 5 min, 10 min, and 15 min were
321 maximized (0.79-0.86) within a window from the 60th-95th percentiles. The optimal rainfall threshold for flash floods (based
322 on regressions of Q as a function of I_D^j) increased from 10.1 mm/hr of I_{60}^{89} (the 89th percentile of 60 min peak rainfall field) in
323 year 1 to 44.6 mm/hr of I_{15}^{90} (the 90th percentile of 15 min peak rainfall field) in year 5 (Figure 4; Table 2). More generally,
324 averaging rainfall intensity over a duration of 15 minutes and choosing a percentile, j , of approximately 75-90 produced an R^2
325 of approximately 0.80 or greater for all post-fire years (Figure 3). None of the other rainfall summary metrics performed this
326 well across all post-fire years.

327

328 **Table. 2 The linear regression-based optimal rainfall ID metrics and corresponding rainfall thresholds for flash floods**
329 **in post-fire years 1-5**

330

331 **Table. 3 The ROC-based optimal metrics of rainfall ID and corresponding rainfall thresholds for flash floods in post-**
332 **fire year 1-5**

333

334 Thresholds derived using the ROC method yielded broadly similar trends. The maximum threat score, TS_{max} , generally
335 increased with j up to a point (approximately $j=90$) and then began to decrease regardless of the choice of duration (D) (Figure
336 6). The highest threat scores (TS), regardless of post-fire year or duration, were generally associated with the 70th-95th

337 percentiles. For events in years 1-2, $TS_{\max}(0.90)$ occurs between I_{60}^{76} and I_{60}^{86} (the 76th -86th percentile of the peak I_{60} rainfall
338 field); for events in years 3-5, the $TS_{\max}(0.94-0.96)$ occurs around I_{30}^{75} (the 75th percentile of the peak I_{30} rainfall field). The
339 optimal rainfall threshold for a flash flood increased from $I_{60}^{86} = 12.9$ mm/hr (the 86th percentile of 60 min peak rainfall field)
340 in year 1 to $I_{30}^{76} = 34.9$ mm/hr (the 76th percentile of 30 min peak rainfall field) in year 5 (Table 3; Figure 6). Averaging
341 rainfall intensity over a duration of 30 minutes and choosing a percentile, j , of approximately 75-90 leads to threat scores of
342 approximately 0.8 or greater for all post-fire years. Other metrics did not perform this well, on average, across all post-fire
343 years.

344 4.2 Increases in rainfall intensity thresholds with time since fire

345 The rainfall intensity thresholds at each percentile increased substantially from post-fire year 1 to 5 (Figures 4 and 7). However,
346 the increase from year 1 to 2 is considerably larger than that from year 2 to 3 or from year 3 to year 5. Taking the I_{30}^{75} (the 75th
347 percentile of the peak I_{30} rainfall field) as an example due to its strong performance as a threshold for all post-fire years, the
348 thresholds based on linear regression analyses in year 1, 2, 3, and 5 are 16.8, 23.2, 26.9, and 27.6 mm/hr, respectively; the
349 ROC-based I_{30}^{75} thresholds in year 1, 2, 3, and 5 are 16.0, 26.9, 32.6, and 34.5 mm/hr, respectively (Figure 7).

350
351 We are also able to use the model to assess the individual impacts of temporal changes in K_{sh} and n_c on temporal variations in
352 the flash flood threshold. If K_{sh} is allowed to vary from year to year (Table 1) and n_c is held fixed at its calibrated value for
353 year 1, then ROC analysis indicates that the optimal threshold of I_{30}^{75} still increases with time since burning (Figure 8).
354 However, it increases slower than the case where both K_{sh} and n_c are allowed to vary with time (Figure 8). If n_c is allowed to
355 vary from year to year (Table 1) and K_{sh} is held fixed at its calibrated value for year 1, then ROC analysis indicates that the
356 optimal threshold associated with I_{30}^{75} increases from year 1 to year 2 but then stays roughly constant as time increases (Figure
357 8). Therefore, changes in K_{sh} and n_c both play important roles in determining the degree to which the flash flood threshold
358 increases from year 1 to year 2, but further increases in the threshold in years three through five are driven mainly by increases
359 in K_{sh} as a function of time since burning.

360
361 **Figure 8: The ROC (receiver operating characteristic) based thresholds for I_{30}^{75} in each year with different model**
362 **settings. Pairs of K_{sh} (saturated hydraulic conductivity on hillslopes) and n_c (Manning s n in channels) in each model**
363 **are along with the data points.**

364 5 Discussion

365 5.1 Optimal metrics of rainfall intensity and duration for flood warning

366 Rain gage records, which provide rainfall intensity data at a single point, are often used to define rainfall ID thresholds in
367 debris-flow and flash flood studies (e.g. Moody and Martin, 2001; Cannon et al., 2008; Cannon et al., 2011; Guzzetti et al.,
368 2008; Kean et al., 2011; Staley et al., 2013; Raymond et al., 2020; McGuire and Youberg, 2020). Using point source data to
369 define thresholds for debris flows and flash floods is ideal when rainfall intensity does not vary substantially over the
370 watershed, an assumption that is most appropriate for watershed areas less than several square kilometers. Radar-derived
371 rainfall data has the advantage of providing spatially explicit information over an entire watershed at a high-temporal resolution
372 (e.g. 5 minute). However, one challenge in using radar-derived precipitation to define thresholds is the need to condense
373 spatially and temporally variable rainfall intensity information down to a single rainfall intensity metric. Regardless of whether
374 the approach to determining an ID threshold involves fitting empirical relationships (e.g., Moody and Martin, 2001; Cannon
375 et al., 2008) or using ROC analysis (e.g., Staley et al., 2013), a single metric is required to represent the rainfall intensity for
376 each duration.

377
378 We summarized spatially variable rainfall intensity data over the watershed by computing the peak value of $I_D^j(t)$, the j^{th}
379 percentile of $I_D(t)$ for each rainstorm. We used two different techniques, one based on a linear regression analysis and one
380 based on ROC analysis (Figure 2), to define thresholds for flash floods in post-fire years 1, 2, 3, and 5. Although the optimal
381 metrics produced by the two approaches are not identical, they are generally similar in each post-fire year. In particular, high
382 R^2 and TS_{max} values are associated with metrics of the peak 75th-85th percentile of rainfall intensity averaged over 15-60 minutes
383 (I_D^j for $75 \leq j \leq 85, D = 15, 30, 60$). In other words, a good indicator of the potential for a flash flood is the presence of
384 intense pulses of rainfall over durations of 15-60 minutes that cover at least 15%-25% of the watershed (Figure 9). This finding
385 highlights the ability of rainstorms to produce flash floods even if they don't cover the majority of the watershed with intense
386 rainfall. If rainfall over the majority of the watershed was required to produce flash floods, then we would expect that I_D^j with
387 $j < 50$ would be a better predictor of flash floods.

388
389 Previous work has also identified that 30-minute rainfall intensity works well for predicting flash floods and debris flows
390 (Moody and Martin, 2001; Kean et al., 2011; Staley et al., 2013). The finding that I_{15}^j, I_{30}^j and I_{60}^j work best as thresholds when
391 $75 \leq j \leq 85$ could be helpful when issuing flash flood warnings based on radar-derived precipitation estimates or data from
392 several real-time rain gages within a watershed. Current operational forecast models such as the High Resolution Rapid Refresh
393 model have a horizontal resolution of 3 km and minimum temporal resolution of 15 minutes (Benjamin et al., 2016; NOAA
394 2021a), such that it is feasible to use either I_{15}^j, I_{30}^j or I_{60}^j in an operational forecast setting. Where sufficient operational
395 NEXRAD weather radar coverage is present, radar-derived precipitation estimates such as the MRMS (Zhang et al., 2016) can

396 provide near-real-time precipitation estimates at 1 km and as fine as 15 min temporal resolution (NOAA 2021b). In the case
397 of poor radar coverage, gap-filling radars may be temporarily deployed or installed (e.g., Jorgensen et al., 2011; Cifelli et al.,
398 2018) to provide information necessary for accurate precipitation estimates. While the magnitude of rainfall thresholds
399 estimated here may only work for similar, recently burned watersheds within the San Gabriel Mountains, this work provides
400 a general methodology for exploring reliable predictors of post-fire flash floods for other watersheds and settings. Further
401 testing is needed in watersheds with different watershed size, topographic characteristics, landscape, and burn severity patterns.
402

403 **Figure 9: Snapshots of the spatial patterns of I_{30}^{75} of 34 unique storms. The peak j^{th} percentile of I_D (rainfall intensity
404 over a duration D) is denoted as I_D^j . I_{30}^{75} is the peak value of the 75st percentile of I_{30} (rainfall intensity over 30-min).
405 Red contours delineate the pixels with rainfall intensities larger than I_{30}^{75} of each storm.**
406

407 Several limitations are present in this work. First, we assess a small number of storm events (34) in the area as we are limited
408 by the length of radar and gage records as well as and the number of events that impact the indicator rain gages, though
409 applying the five Z-R relationships provides us with 170 rainfall realizations to assess. We prefer the use of observed rainfall
410 data (radar and gauges) over simulated products, such as output from a rainfall generator (e.g., Zhao et al., 2019; Evin et al.,
411 2018), as the radar is able to capture the spatial and temporal patterns of rainfall intensity in the study area's complex terrain.
412 Though rainfall generators have advanced to represent some synoptic-to-mesoscale features, such as frontal and convective
413 precipitation (e.g., Zhao et al. 2019), they are fundamentally designed to represent statistical characteristics of rainfall in places
414 with limited observations (Wilks and Wilby 1999) and cannot be relied upon to replicate small scale storm characteristics in
415 complex terrain (e.g., Camera et al. 2016). Future work could compare results from this hydrologic modeling experiment with
416 observed versus simulated rainfall. Second, the challenges of Z-R relationships to convert reflectivity to precipitation also
417 presents challenges in accurately representing precipitation values. This can be addressed in future work through studies to
418 constrain Z-R relationships for storms producing intense rainfall in this region and through the deployment or installation of
419 high-resolution gap-filling radars (e.g., Johnson et al., 2019).

420 5.2 The role of hydrological models in rainfall intensity threshold estimation

421 In this study we employed the K2 model calibrated by Liu et al. (2021) to parameterize hydrologic changes affecting Hortonian
422 overland flow within a five-year period following fire. Hillslope saturated hydraulic conductivity ($K_{sh} = 7.2$ mm/hr) and
423 hydraulic roughness in channels ($n_c = 0.087$ s/m^{1/3}) were lowest immediately after fire (Table 1), resulting in high runoff
424 coefficients and low rainfall thresholds in post-fire year 1. In later years, with K_{sh} and n_c gradually increasing (Table 1), more
425 rainfall infiltrated into soil and there was increased attenuation of flood peaks. Simulations indicate that the number of flash-
426 flood-producing rainstorms decreased from 59 in year 1 to 25, 18, and 16 in years 2, 3, and 5, respectively. Runoff coefficients
427 and peak discharge of simulated hydrographs also decreased with time since fire (Figure 10). Given the same precipitation

428 ensemble, the likelihood of flash floods significantly decreased with time. The peak discharge produced by the highest intensity
429 rainfall event with I_{60}^{75} of 51.8 mm/hr was 554.0 m³/s in the first year after the fire, which is three times greater than the peak
430 discharges of 157.5 m³/s in year 3 and 161.2 m³/s in year 5 produced by the same rainstorm. From a flood hazard perspective,
431 the downstream area may be exposed to a 1000-year flood under the recently burned condition (less than one year since the
432 fire), whereas the discharge produced in years three and five would amount to roughly a 30- to 40-year flood (Figure S3).

433

434 **Figure 10: Box plots showing the runoff coefficient and peak discharge of flash floods in post-fire year 1, 2, 3, and 5.**
435 **The numbers of flash floods in each year are displayed next to the box.**

436 We were also able to perform numerical experiments to quantify the relative importance of temporal changes in K_{sh} and n_c on
437 temporal variations in the flash flood threshold (Figure 8). Results suggest that changes in vegetation and grain roughness,
438 which are likely to influence n_c , throughout the recovery process are less important for determining flash flood potential in our
439 study area relative to changes to saturated hydraulic conductivity on hillslopes. It is worth noting that temporal changes in
440 other model parameters (e.g., hydraulic roughness on hillslopes, capillary drive) may play more of a role in driving changes
441 in post-fire flash flood thresholds in other settings. In this study, however, we focus on changes in K_{sh} and n_c because Liu et
442 al. (2021) were able to detect temporal changes in n_c and K_{sh} through time and unable to detect similar temporal changes in
443 other hydrologic parameters (e.g., hydraulic roughness on hillslopes, capillary drive) due to their relatively minor influence on
444 runoff in the study watershed.

445

446 In this study, the optimal flash flood thresholds increased from $I_{30}^{75} = 16.0$ -16.8 mm/hr in post-fire year 1, to 23.2-26.9 mm/hr
447 in year 2, and 27.6-34.5 mm/hr in post-fire year 5 (Figure 4 and 7; Table 2-3). In the San Gabriel Mountains and nearby San
448 Bernardino and San Jacinto Mountains, Cannon et al. (2008) estimated rainfall thresholds of $I_{30} = 9.5$ mm/hr for flash floods
449 and debris flows in the first winter rainy season following fire. They found that the thresholds for flash floods and debris flows
450 increased to $I_{30} = 19.8$ mm/hr in post-fire year 2. The thresholds that we infer from hydrological modeling are greater than those
451 reported by Cannon et al. (2008), which may be partly due to differences in (1) data and methods used and (2) the size of the
452 studied watersheds. Our results are driven by a hydrologic model, forced with a radar precipitation ensemble that consists of
453 170 rainstorms that contain a variety of storm types that impact southern California. The occurrence of a flash flood is based
454 on exceedance of the maximum channel capacity and we summarize temporal changes in the rainfall ID threshold using I_{30}^{75}
455 since we find this to be a reliable metric for all post-fire years included in this study. In contrast, Cannon et al. (2008)
456 established rainfall ID relations by using observations of rainstorms and hydrological response in the two years following fire
457 in 87 small watersheds (0.2-4.6 km²). They base their thresholds on rainfall characteristics that produced either flash floods or
458 debris flows whereas we focus solely on flash floods. In their dataset, flash floods and debris flows were identified by
459 investigating flood and debris flow deposits at the outlet of those small watersheds in the field. Despite differences in the

460 magnitude of the thresholds, the increase in the threshold from post-fire year 1 to year 2 in both studies are quite close. This
461 agreement provides support for the use of simulation-based approaches to inform temporal shifts in rainfall ID thresholds.

462
463 During the recovery process, increasing thresholds for flash floods and debris flows have also been identified in other areas at
464 different scales by either observation- or simulation-based studies, such as hillslopes in the Colorado Front Range (Ebel, 2020)
465 and small watersheds in Australia (Noske et al., 2016). The consistent increase in rainfall ID thresholds with time since fire in
466 different geographic and ecological zones implies that hydraulic and hydrologic models may be useful tools for exploring how
467 transient effects of fire translate into changes in water-related hazards. Particularly when historic data is limited and traditional
468 empirical methods are impractical for defining thresholds, the role of hydraulic and hydrological models becomes more
469 important.

470 **6 Conclusions**

471 We used 250 m, 5-minute radar-derived precipitation estimates over a 41.5 km² watershed in combination with a calibrated
472 hydrological model to estimate rainfall intensity-duration thresholds for post-fire flash floods as a function of time since
473 burning. The main outcomes of this study are 1) identification of optimal radar-derived rainfall metrics for post-fire flash flood
474 prediction in southern California, 2) estimates of temporal changes in rainfall ID thresholds for flash floods following
475 disturbance in a chaparral-dominated ecosystem, and 3) a methodology for using a hydrological model to assess changes in
476 post-fire flash flood thresholds.

477
478 Results indicate that thresholds based on the 75th-85th percentile of peak rainfall intensity averaged over 15-60 minutes perform
479 best at predicting the occurrence of a flash flood in our study area. In other words, a flash flood tends to be produced when
480 rainfall intensity over 15%-25% of the watershed area exceeds a critical value. A threshold based on I_{30}^{75} performs consistently
481 well for post-fire years 1, 2, 3, and 5, although the magnitude of the threshold increases with time since burning. For the
482 watershed studied, the I_{30}^{75} threshold increases from 16.0-16.8 mm/hr for year 1 to 23.2-26.9 mm/hr, 26.9-32.6 mm/hr, and
483 27.6-34.5 mm/hr, for years 2, 3, and 5 respectively. Increases in the threshold value of I_{30}^{75} can be primarily attributed to
484 increases in K_{sh} rather than n_c during the hydrological recovery process. The increase in the magnitude of the threshold from
485 year 1 to year 2 is consistent with previous observations from nearby areas in southern California. Results provide a
486 methodology for using radar-derived precipitation estimates and hydrological modeling to estimate flash flood thresholds for
487 improved warning and mitigation of post-fire hydrologic hazards. Thresholds developed through these methods can then be
488 built into operational tools that use incoming radar data to evaluate flash flood hazard in near-real time or precipitation forecasts
489 to evaluate potential for flash flood hazard in burned watersheds.

490 **Author contributions**

491 TL and LM conceived the study. TL, LM, NO and FC contributed to the development and design of the methodology. TL
492 analyzed and prepared the manuscript with review and analysis contributions from LM, NO and FC.

493 **Competing interests**

494 The authors declare that they have no conflict of interest.

495 **Acknowledgments**

496 Haiyan Wei, Carl L. Unkrich, and David C. Goodrich, who are from the KINEROS2 development group in the USDA ARS
497 Southwest Watershed Research Center in Tucson, helped with the setting up of the KINEROS2 model and ingestion of the
498 RADAR precipitation data into the model. We are thankful for their great help.

499 **Financial support**

500 This work was supported by the National Oceanic and Atmospheric Administration (NOAA) Collaborative Science,
501 Technology, and Applied Research (CSTAR) Program under grant NA19NWS4680004 and by the National Integrated
502 Drought Information System (NIDIS) through Task Order 1332KP20FNRMT0012.

503 **References**

- 504 Bartles, M., Brunner, G., Fleming, M., Faber, B., Karlovits, G., and Slaughter, J.: HEC-SSP Statistical Software Package
505 Version 2.2, June 2019.
- 506 Benjamin, S. G., Weygandt, S. S., Brown, J. M., Hu, M., Alexander, C. R., Smirnova, T. G., Olson, J. B., James, E. P., Dowell,
507 D. C., Grell, G. A., Lin, H., Peckham, S. E., Smith, T. L., Moninger, W. R., Kenyon, J. S., & Manikin, G. S. (2016). A North
508 American Hourly Assimilation and Model Forecast Cycle: The Rapid Refresh, *Monthly Weather Review*, 144(4), 1669-1694.
509 <https://doi.org/10.1175/MWR-D-15-0242.1>
- 510 Camera, C., Bruggeman, A., Hadjinicolaou, P., Michaelides S., & Lange, M. A. (2017). Evaluation of a spatial rainfall
511 generator for generating high resolution precipitation projections over orographically complex terrain. *Stoch Environ Res Risk*
512 *Assess* 31, 757–773. <https://doi.org/10.1007/s00477-016-1239-1>
- 513 Canfield, H. E., Goodrich, D. C., & Burns, I. S. (2005). Selection of parameters values to model post-fire runoff and sediment
514 transport at the watershed scale in southwestern forests. *Proceedings of the 2005 Watershed Management Conference -*
515 *Managing Watersheds for Human and Natural Impacts: Engineering, Ecological, and Economic Challenges*, 40763(June
516 2015), 561–572. [https://doi.org/10.1061/40763\(178\)48](https://doi.org/10.1061/40763(178)48)

517 Cannon, F., and Coauthors, 2020: Observations and Predictability of a High-Impact Narrow Cold-Frontal Rainband over
518 Southern California on 2 February 2019. *Wea. Forecasting*, 35, 2083–2097. <https://doi.org/10.1175/WAF-D-20-0012.1>.

519 Cannon, S. H., Boldt, E. M., Laber, J. L., Kean, J. W., & Staley, D. M. (2011). Rainfall intensity-duration thresholds for
520 postfire debris-flow emergency-response planning. *Natural Hazards*, 59(1), 209–236. [https://doi.org/10.1007/s11069-011-](https://doi.org/10.1007/s11069-011-9747-2)
521 [9747-2](https://doi.org/10.1007/s11069-011-9747-2)

522 Cannon, S. H., Gartner, J. E., Wilson, R. C., Bowers, J. C., & Laber, J. L. (2008). Storm rainfall conditions for floods and
523 debris flows from recently burned areas in southwestern Colorado and southern California. *Geomorphology*, 96, 250–269.
524 <https://doi.org/10.1016/j.geomorph.2007.03.019>

525 Carsel, R. F., & Parrish, R. S. (1988). Developing joint probability distributions of soil water retention characteristics. *Water*
526 *Resources Research*, 24(5), 755–769. <https://doi.org/10.1029/WR024i005p00755>

527 Cifelli, R., Chandrasekar, V., Chen, H., & Johnson, L. E. (2018). High resolution radar quantitative precipitation estimation in
528 the San Francisco Bay Area: Rainfall monitoring for the urban environment. *Journal of the Meteorological Society of Japan*.
529 *Ser. II*, 96, 141-155.

530 Dyrness, C. (1976), Effect of Wildfire on Soil Wettability in the High Cascades of Oregon, U.S. Dept. of Agriculture, Forest
531 Service, Pacific Northwest forest and Range Experiment Station, Portland, Oreg.

532 Ebel, B. A. (2020). Temporal evolution of measured and simulated infiltration following wildfire in the Colorado Front Range,
533 USA: Shifting thresholds of runoff generation and hydrologic hazards. *Journal of Hydrology*, 585(March), 124765.
534 <https://doi.org/10.1016/j.jhydrol.2020.124765>

535 Ebel, B. A., & Martin, D. A. (2017). Meta - analysis of field - saturated hydraulic conductivity recovery following wildland
536 fire: Applications for hydrologic model parameterization and resilience assessment. *Hydrological Processes*. 2017; 31: 3682–
537 3696. <https://doi.org/10.1002/hyp.11288>

538 Ebel, B. A., & Moody, J. A. (2013). Rethinking infiltration in wildfire-affected soils. *Hydrological Processes*, 27(10), 1510–
539 1514. <https://doi.org/10.1002/hyp.9696>

540 Ebel, B. A., & Moody, J. A. (2017). Synthesis of soil-hydraulic properties and infiltration timescales in wildfire-affected soils.
541 *Hydrological Processes*, 31(2), 324–340. <https://doi.org/10.1002/hyp.10998>

542 Evin, G., Favre, A.-C., & Hingray, B. (2018). Stochastic generation of multi-site daily precipitation focusing on extreme
543 events, *Hydrol. Earth Syst. Sci.*, 22, 655–672. <https://doi.org/10.5194/hess-22-655-2018>.

544 Gillett NP, Weaver AJ, Zwiers FW, Flannigan MD. (2004). Detecting the effect of climate change on Canadian forest fires.
545 *Geophysical Research Letters* 31. <https://doi-org.ezproxy2.library.arizona.edu/10.1029/2004>

546 Goodrich, D. C., Burns, I. S., Unkrich, C. L., Semmens, D. J., Guertin, D. P., Hernandez, M. (2012). KINEROS2/AGWA:
547 Model use, Calibration, and Validation. *Transactions of the ASABE*, 55(4), 1561–1574. <https://doi.org/10.13031/2013.42264>

548 Guzzetti, F., Peruccacci, S., Rossi, M., & Stark, C. P. (2008). The rainfall intensity-duration control of shallow landslides and
549 debris flows: An update. *Landslides*, 5(1), 3–17. <https://doi.org/10.1007/s10346-007-0112-1>

550 Hubbert, K. R., & Oriol, V. (2005). Temporal fluctuations in soil water repellency following wildfire in chaparral steep-lands,
551 southern California. *International Journal of Wildland Fire*, 14(4), 439–447. <https://doi.org/10.1071/WF05036>

552 Hubbert, K. R., Wohlgemuth, P. M., & Beyers, J. L. (2012). Effects of hydromulch on post-fire erosion and plant recovery in
553 chaparral shrublands of southern California. *International Journal of Wildland Fire*, 21(2), 155–167.
554 <https://doi.org/10.1071/WF10050>

555 Huffman, E. L., MacDonald, L. H., & Stednick, J. D. (2001). Strength and persistence of fire-induced soil hydrophobicity
556 under ponderosa and lodgepole pine, Colorado Front Range. *Hydrological Processes*, 15(15), 2877–2892.
557 <https://doi.org/10.1002/hyp.379>

558 Johnson, LE, Cifelli, R, White, A. Benefits of an advanced quantitative precipitation information system. *J Flood Risk*
559 *Management*. 2020; 13 (Suppl. 1):e12573. <https://doi.org/10.1111/jfr3.12573>

560 Jorgensen, D. P., Hanshaw, M. N., Schmidt, K. M., Laber, J. L., Staley, D. M., Kean, J. W., & Restrepo, P. J. (2011). Value
561 of a dual-polarized gap-filling radar in support of southern California post-fire debris-flow warnings. *Journal of*
562 *Hydrometeorology*, 12(6), 1581-1595.

563 Kean, J. W., Staley, D. M., & Cannon, S. H. (2011). In situ measurements of post-fire debris flows in southern California:
564 Comparisons of the timing and magnitude of 24 debris-flow events with rainfall and soil moisture conditions. *Journal of*
565 *Geophysical Research: Earth Surface*, 116(4), 1–21. <https://doi.org/10.1029/2011JF002005>

566 Kean, J. W., Staley, D. M., & Cannon, S. H. (2011). In situ measurements of post-fire debris flows in southern California:
567 Comparisons of the timing and magnitude of 24 debris-flow events with rainfall and soil moisture conditions. *Journal of*
568 *Geophysical Research: Earth Surface*, 116(4), 1–21. <https://doi.org/10.1029/2011JF002005>

569 Kitzberger, T., Falk, D. A., Westerling, A. L., & Swetnam, T. W. (2017). Direct and indirect climate controls predict
570 heterogeneous early-mid 21st century wildfire burned area across western and boreal North America. *PLoS ONE*, 12(12), 1–
571 24. <https://doi.org/10.1371/journal.pone.0188486>

572 Lamb, M. P., Scheingross, J. S., Amidon, W. H., Swanson, E., & Limaye, A. (2011). A model for fire-induced sediment yield
573 by dry ravel in steep landscapes. *Journal of Geophysical Research: Earth Surface*, 116(3), 1–13.
574 <https://doi.org/10.1029/2010JF001878>

575 Larsen, I. J., MacDonald, L. H., Brown, E., Rough, D., Welsh, M. J., Pietraszek, J. H., et al. (2009). Causes of post-fire runoff
576 and erosion: Water repellency, cover, or soil sealing? *Soil Science Society of America Journal*, 73(4), 1393–1407.
577 <https://doi.org/10.2136/sssaj2007.0432>

578 Leopold, L.B., Wolman, M.G., and Miller, J.P. 1964. *Fluvial Processes in Geomorphology*. Dover, New York.

579 Liu, T., McGurire, L. A., Wei, H. Y., Rengers, F. K., Gupta, H., Ji, L., Goodrich, D. C. (2021). The timing and magnitude of
580 changes to Hortonian overland flow at the watershed scale during the post-fire recovery process. *Hydrological Processes*.
581 35(5). <https://doi.org/10.1002/hyp.14208>

582 Marshall, J. S., and W. M. K. Palmer, 1948: The distribution of raindrops with size. *J. Meteor.*, 5, 165–166,
583 [https://doi.org/10.1175/1520-0469\(1948\)005<0165:TDORWS>2.0.CO;2](https://doi.org/10.1175/1520-0469(1948)005<0165:TDORWS>2.0.CO;2).

584 McGuire, L. A., & Youberg, A. M. (2020). What drives spatial variability in rainfall intensity-duration thresholds for post-
585 wildfire debris flows? Insights from the 2018 Buzzard Fire, NM, USA. *Landslides*, December 2019.
586 <https://doi.org/10.1007/s10346-020-01470-y>

587 Meles, M .B., Goodrich, D. C., Gupta, H. V., Burns, S. I, Unkrich, C. L., Razavi, S., Guertin, D. P. (2019). Uncertainty and
588 parameter sensitivity of the KINEROS2 physically-based distributed sediment and runoff model. In *Federal Interagency*
589 *Sedimentation and Hydrologic Modeling Conference*.

590 Miller, S. N., Semmens, D. J., Goodrich, D. C., Hernandez, M., Miller, R. C., Kepner, W. G., & Guertin, D. P. (2007). The
591 automated geospatial watershed assessment tool. 851 *Environmental Modelling and Software*. 22(3), 365-377. 852
592 <https://doi.org/10.1016/j.envsoft.2005.12.004>

593 Moody, J. A., & Ebel, B. A. (2012). Hyper-dry conditions provide new insights into the cause of extreme floods after wildfire.
594 *Catena*, 93, 58–63. <https://doi.org/10.1016/J.CATENA.2012.01.006>

595 Moody, J. A., & Martin, D. A. (2001). Post-fire, rainfall intensity – peak discharge relations for three mountainous watersheds
596 in the western USA. 2993(July), 2981–2993. <https://doi.org/10.1002/hyp.386>

597 Moreno, H. A., Gourley, J. J., Pham, T. G., & Spade, D. M. (2020). Utility of satellite-derived burn severity to study short-
598 and long-term effects of wildfire on streamflow at the basin scale. *Journal of Hydrology*, 580(October 2019), 124244.
599 <https://doi.org/10.1016/j.jhydrol.2019.124244>

600 NOAA National Weather Service (NWS) Radar Operations Center (1991): NOAA Next Generation Radar (NEXRAD) Level
601 2 Base Data. NOAA National Centers for Environmental Information. doi:10.7289/V5W9574V

602 NOAA. (2021a). High-Resolution Rapid Refresh (HRRR) Model [Dataset]. <https://registry.opendata.aws/noaa-hrrr-pds/>

603 NOAA. (2021b) Multi-Radar/Multi-Sensor System (MRMS). [Dataset]. <https://www.nssl.noaa.gov/projects/mrms/>

604 Noske, P. J., Nyman, P., Lane, P. N. J., & Sheridan, G. J. (2016). Effects of aridity in controlling the magnitude of runoff and
605 erosion after wildfire. *Water Resources Research*, 52(6), 4338–4357. <https://doi.org/10.1002/2015WR017611>

606 Oakley, N. S., Lancaster, J. T., Kaplan, M. L., & Ralph, F. M. (2017). Synoptic conditions associated with cool season post-
607 fire debris flows in the Transverse Ranges of southern California. *Natural Hazards*, 88(1), 327–354.
608 <https://doi.org/10.1007/s11069-017-2867-6>

609 Oakley, N. S., J. T. Lancaster, B. J. Hatchett, J. Stock, F. M. Ralph, S. Roj, & S. Lukashov. (2018a). A 22-Year climatology
610 of cool season hourly precipitation thresholds conducive to shallow landslides in California. *Earth Interact.*, 22, 1–35,
611 <https://doi.org/10.1175/EI-D-17-0029.1>.

612 Oakley, N. S., Cannon, F., Munroe, R., Lancaster, J. T., Gomberg, D., & Ralph, F. M. (2018b). Brief communication:
613 Meteorological and climatological conditions associated with the 9 January 2018 post-fire debris flows in Montecito and
614 Carpinteria, California, USA. *Natural Hazards and Earth System Sciences*, 18(11), 3037-3043. [https://doi.org/10.5194/nhess-](https://doi.org/10.5194/nhess-18-3037-2018)
615 [18-3037-2018](https://doi.org/10.5194/nhess-18-3037-2018)

616 Parlange, J. Y., Lisle, I., Braddock, R. D., & Smith, R. E. (1982). The three-parameter infiltration equation. *Soil Science*,
617 133(6), 337-341. <https://doi.org/10.1097/00010694-198206000-00001>

618 Raymond, C. A., McGuire, L. A., Youberg, A. M., Staley, D. M., & Kean, J. W. (2020). Thresholds for post-wildfire debris
619 flows: Insights from the Pinal Fire, Arizona, USA. *Earth Surface Processes and Landforms*, 45(6), 1349–1360.
620 <https://doi.org/10.1002/esp.4805>

621 Rengers, F. K., McGuire, L. A., Kean, J. W., Staley, D. M., & Youberg, A. M. (2019). Progress in simplifying hydrologic
622 model parameterization for broad applications to post-wildfire flooding and debris-flow hazards. In *Earth Surface Processes
623 and Landforms* (Vol. 44, Issue 15, pp. 3078–3092). <https://doi.org/10.1002/esp.4697>

624 Saksa, P. C., Bales, R. C., Tobin, B. W., Conklin, M. H., Tague, C. L., & Battles, J. J. (2020). Fuels treatment and wildfire
625 effects on runoff from Sierra Nevada mixed-conifer forests. *Ecohydrology*, 13, 1–16. <https://doi.org/10.1002/eco.2151>

626 Schmidt, K. M., M. N. Hanshaw, J. F. Howle, J. W. Kean, D. M. Staley, J. D. Stock, and G. W. Bawden (2011), Hydrologic
627 conditions and terrestrial laser scanning of post-fire debris flows in the San Gabriel Mountains, CA, U.S.A., in *Debris-Flow
628 Hazards Mitigation, Mechanics, Prediction, and Assessment*, edited by R. Genevois, D. L. Hamilton, and A. Prestininzi, pp.
629 583–593, Casa Editrice Univ. La Sapienza, Rome.

630 Smith, R. E., Goodrich, D. C., Woolhiser, D. A., & Unkrich, C. L. (1995). KINEROS—A kinematic runoff and erosion model.
631 In VijayP. Singh (Ed.), *Computer models of watershed hydrology* (p. 1130). Fort Collins, CO: Water Resources Publications.

632 Staley, D. M., Kean, J. W., Cannon, S. H., Schmidt, K. M., & Laber, J. L. (2013). Objective definition of rainfall intensity-
633 duration thresholds for the initiation of post-fire debris flows in southern California. *Landslides*, 10(5), 547–562.
634 <https://doi.org/10.1007/s10346-012-0341-9>

635 Staley, D.M., Wasklewicz, T.A. and Kean, J.W., 2014, Characterizing the primary material sources and dominant erosional
636 processes for post-fire debris-flow initiation in a headwater basin using multi-temporal terrestrial laser scanning data:
637 *Geomorphology*, v. 214, 324-338.

638 Staley, D. M., Negri, J. A., Kean, J. W., Laber, J. L., Tillery, A. C., & Youberg, A. M. (2017). Prediction of spatially explicit
639 rainfall intensity–duration thresholds for post-fire debris-flow generation in the western United States. *Geomorphology*, 278,
640 149–162. <https://doi.org/10.1016/j.geomorph.2016.10.019>

641 Stoof, C. R., Vervoort, R. W., Iwema, J., Ferreira, A. J. D., Ritsema, C. J., Group, D., Resources, N., Water, Q., Group, M., &
642 Green, A. (2012). Hydrological response of a small catchment burned by experimental fire. 267–285.
643 <https://doi.org/10.5194/hess-16-267-2012>

644 Sweeney, T. L. (1992). Modernized areal flash flood guidance. *NOAA Technical Memorandum, NWS HYDRO*, 44.

645 Tang, H., McGuire, L. A., Rengers, F. K., Kean, J. W., Staley, D. M., & Smith, J. B. (2019). Evolution of Debris-Flow Initiation
646 Mechanisms and Sediment Sources During a Sequence of Postwildfire Rainstorms. *Journal of Geophysical Research: Earth
647 Surface*, 124(6), 1572–1595. <https://doi.org/10.1029/2018JF004837>

648 USDA Forest Service (2009). Station fire burned area emergency response (BAER). unpublished Report. Available:
649 http://www.fs.usda.gov/Internet/FSE_DOCUMENTS/stelprdb5245056.pdf

650 Watson, C. L., & Letey, J. (1970). Indices for Characterizing Soil-Water Repellency Based upon Contact Angle-Surface
651 Tension Relationships. *Soil Science Society of America Journal*, 34(6), 841–844.
652 <https://doi.org/10.2136/sssaj1970.03615995003400060011x>

653 Wilks, D. S., & Wilby, R. L. (1999). The weather generation game: a review of stochastic weather models. *Progress in Physical
654 Geography: Earth and Environment*, 23(3), 329–357. <https://doi.org/10.1177/030913339902300302>

655 Westerling AL, Hidalgo HG, Cayan DR, Swetnam TW. 2006. Warming and earlier spring increase western US forest wildfire
656 activity. *Science* 313: 940–943.

657 Wilson, C., Kampf, S. K., Wagenbrenner, J. W., & Macdonald, L. H. (2018). Forest Ecology and Management Rainfall
658 thresholds for post- fire runoff and sediment delivery from plot to watershed scales. *Forest Ecology and Management*, 430,
659 346–356. <https://doi.org/10.1016/j.foreco.2018.08.025>

660 Yatheendradas, S., Wagener, T., Gupta, H., Unkrich, C., Goodrich, D., Schaffner, M., & Stewart, A. (2008). Understanding
661 uncertainty in distributed flash flood forecasting for semiarid regions. *Water Resources Research*, 44(5), 1–17.
662 <https://doi.org/10.1029/2007WR005940>

663 Zhang, J., Howard, K., Langston, C., Kaney, B., Qi, Y., Tang, L., Grams, H., Wang, Y., Cocks, S., Martinaitis, S., Arthur, A.,
664 Cooper, K., Brogden, J., & Kitzmiller, D. (2016). Multi-Radar Multi-Sensor (MRMS) Quantitative Precipitation Estimation:
665 Initial Operating Capabilities, *Bulletin of the American Meteorological Society*, 97(4), 621-638.
666 <https://journals.ametsoc.org/view/journals/bams/97/4/bams-d-14-00174.1.xml>

667 Zhao, Y., Nearing, M.A., & Guertin, D.P., 2019. A daily spatially explicit stochastic rainfall generator for a semi-arid climate.
668 *J. Hydrol.* 574, 181–192.

669

671
672
673
674

Table 1. Summary of model parameters for post-fire year 1, 2, 3, and 5. The saturated hydraulic conductivity on hillslopes (K_{sh}) and hydraulic roughness in channels (n_c) are the average of values calibrated in post-fire years 1, 2, 3, and 5 (Liu et al., 2021)

Post-fire Year	Calibration Events	K_{sh} (mm/hr)	n_c (s/[m ^{1/3}])
1	12 Dec 2009	7.2	0.087
	17 Jan 2010		
	5 Feb 2010		
2	17 Dec 2010	13.8	0.275
	20 Mar 2011		
3	17 Mar 2012	18.5	0.320
	13 Apr 2012		
5	28 Feb 2014	23.8	0.280

675
676

677 **Table. 2 The linear regression-based optimal rainfall ID metrics and corresponding rainfall thresholds for flash floods**
 678 **in post-fire years 1-5**

Year	Rainfall metric	Equation	R^2_{\max} (95% CI)	Intensity (mm/hr) (95% CI)
1	I_{60}^{89}	$Q = 8.51 * I_{60}^{89} - 70.19$	0.89 (0.80, 0.92)	15.05 (14.50, 15.53)
2	I_{15}^{88}	$Q = 0.94 * I_{15}^{88} - 14.86$	0.86 (0.73, 0.92)	39.23 (36.97, 41.84)
3	I_{15}^{90}	$Q = 0.63 * I_{15}^{90} - 11.41$	0.86 (0.76, 0.93)	49.87 (36.68, 55.44)
5	I_{15}^{90}	$Q = 0.60 * I_{15}^{90} - 11.51$	0.86 (0.70, 0.92)	51.64 (48.18, 60.13)

679 Note: We denote the peak j^{th} percentile of I_D (rainfall intensity over a duration D) as I_D^j . For example, I_{15}^{88} is the peak value of
 680 the 88th percentile of I_{15} (rainfall intensity over 15-min).
 681
 682

683 **Table. 3 The ROC-based optimal metrics of rainfall ID and corresponding rainfall thresholds for flash floods in post-**
 684 **fire year 1-5**

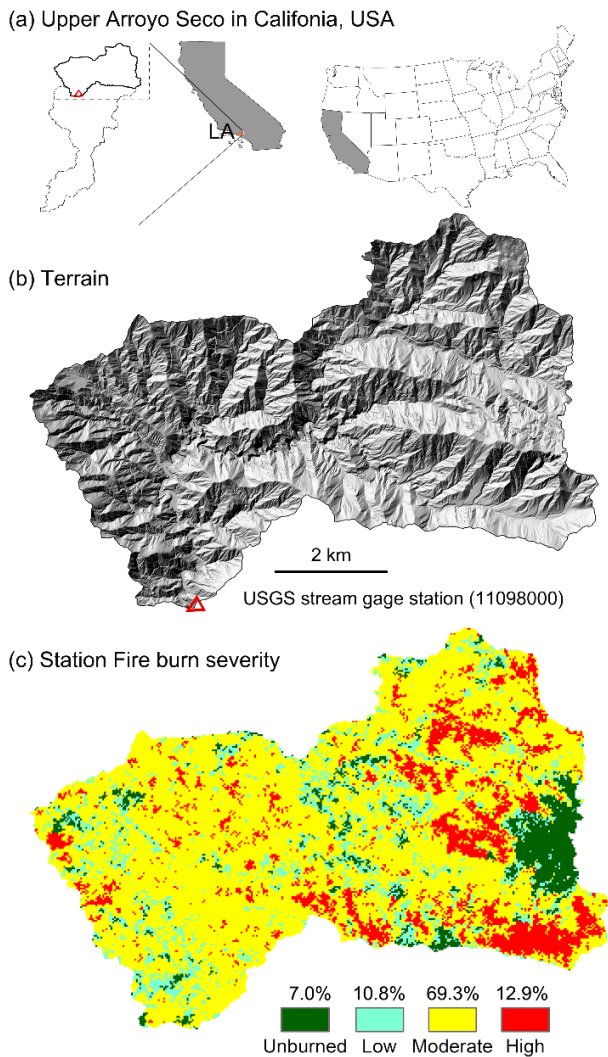
Year	Rainfall metric	TS _{max} (95% CI)	Intensity (mm/hr) (95% CI)
1	I_{60}^{86}	0.90 (0.84, 0.96)	12.91 (12.20, 13.20)
2	I_{60}^{76}	0.90 (0.74, 0.99)	19.98 (17.80, 20.40)
3	I_{30}^{75}	0.94 (0.78, 1.00)	32.60 (28.64, 33.60)
5	I_{30}^{76}	0.96 (0.82, 1.00)	34.86 (32.20, 35.40)

685
 686 Note: We denote the peak j^{th} percentile of I_D (rainfall intensity over a duration D) as I_D^j . For example, I_{60}^{86} is the peak value of
 687 the 86th percentile of I_{60} (rainfall intensity over 60-min).
 688

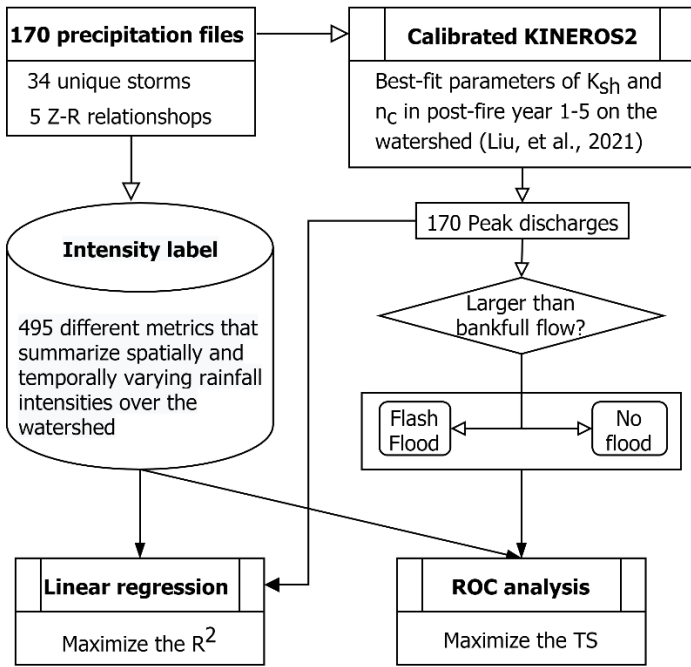
689

Figures and captions

690

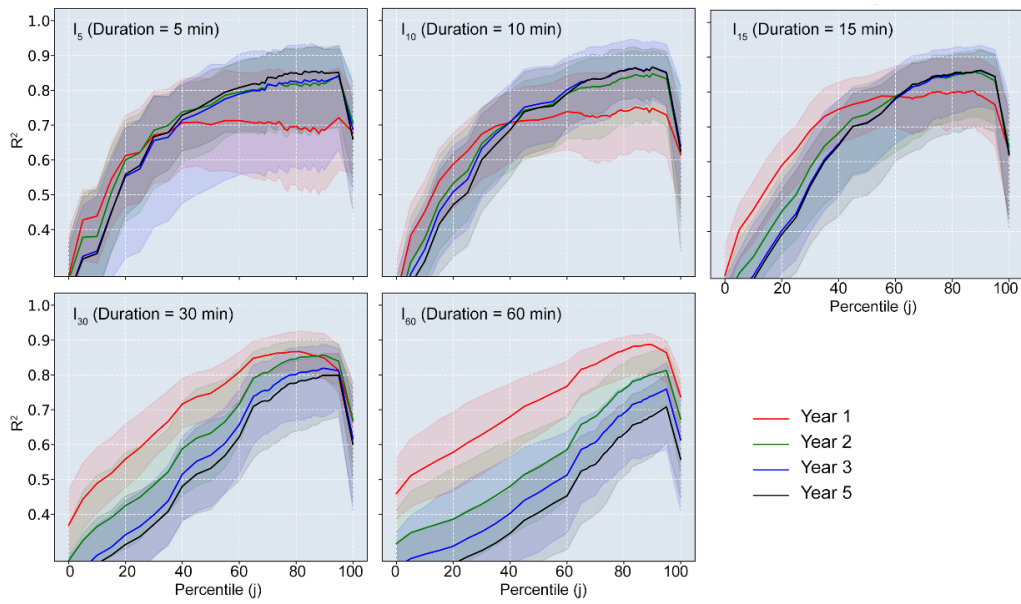


692 **Figure 1: Modified from figure 1 in Liu et al. (2021) (a) The location of the upper Arroyo Seco watershed within California. The red**
 693 **triangle indicates the location of the USGS stream gage (11098000); (b) Shaded relief showing the study watershed with the USGS**
 694 **stream gage (red triangle; 34°13 20", -118°10 36"); (c) Soil burn severity for the 2009 Station fire. Burn severity percentages are for**
 695 **planform area within each category.**
 696

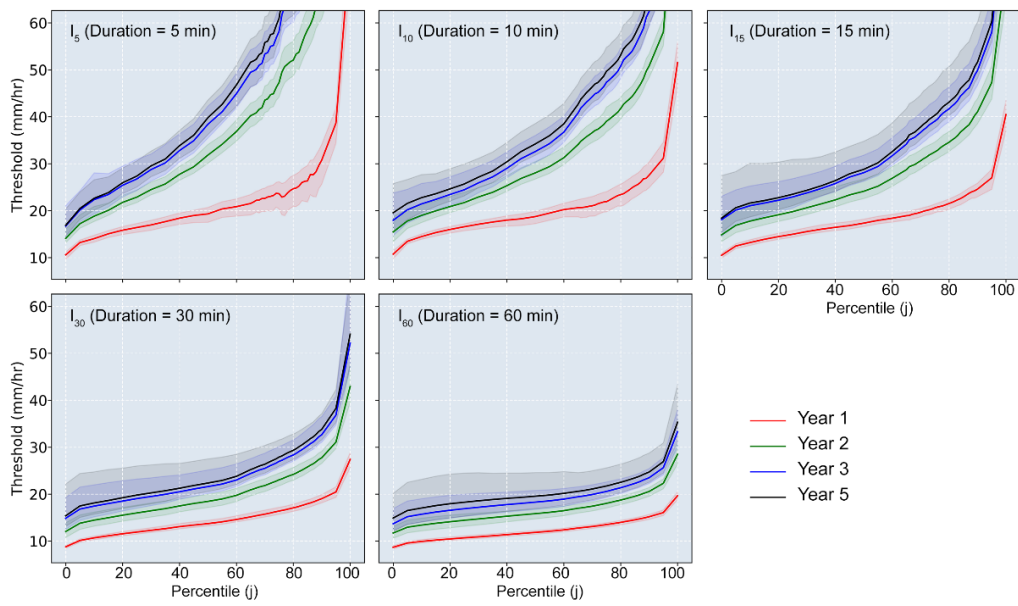


698 **Figure 2: Delineation of rainfall intensity-duration threshold for post-fire flash flood**

699

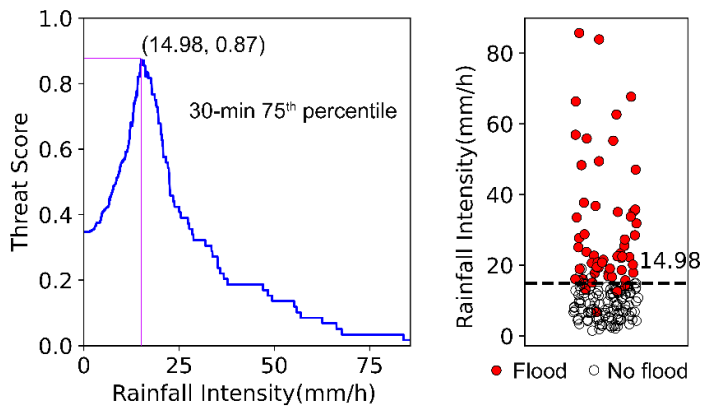


701 **Figure 3: The determination coefficient (R^2) and 95% confidence interval associated with the linear regression between**
 702 **I_D^j and peak discharge in post-fire year 1, 2, 3, and 5. Data used to fit the linear relation are from events with peak**
 703 **discharge greater than $2 \text{ m}^3/\text{s}$.**
 704



706 **Figure 4: The rainfall intensity-duration threshold for flash flood derived from the best linear relation for different**
 707 **durations and percentiles of the most intense rainfall field in post-fire year 1, 2, 3, and 5.**

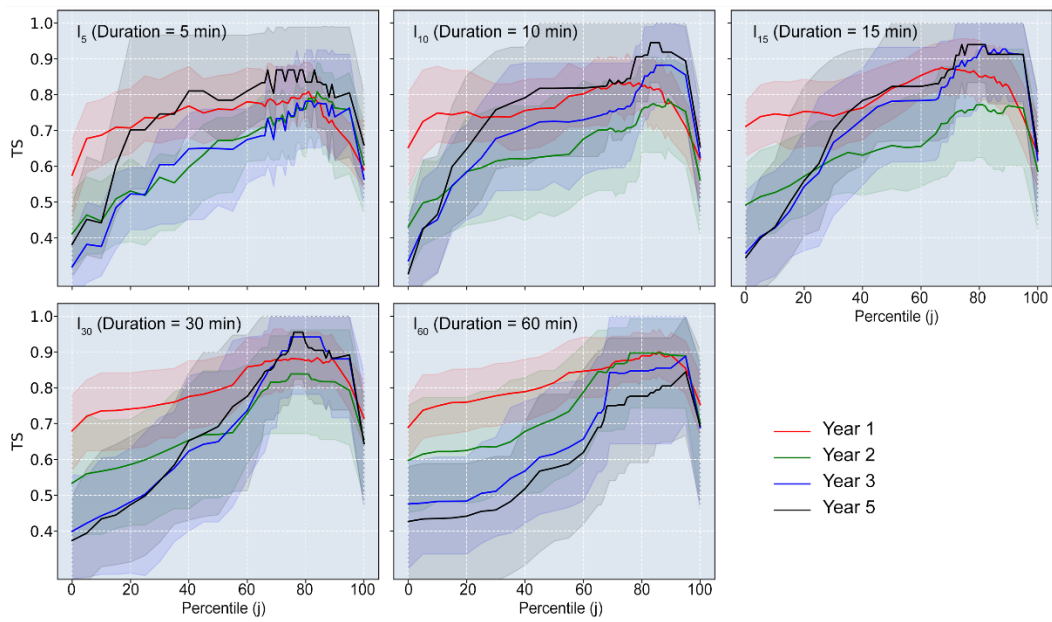
708



710

711 **Figure 5: Threat score (TS) of the peak 75th percentile of I_{30} in post-fire year 1. (a) Relationship between rainfall**
 712 **intensity and TS; (b) Scatter plots of positive (flood, red circle) and negative (no flood, hollow circle) with the rainfall**
 713 **intensity associated with the maximum TS.**

714

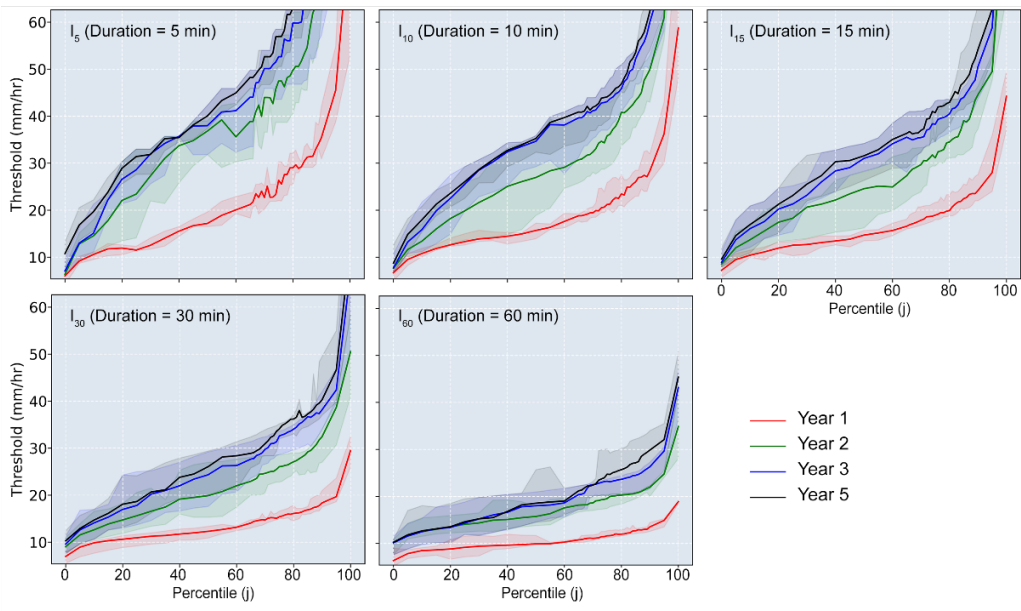


716

717 **Figure 6: The threat scores (TS_{\max}) associated with flood occurrence and I_D^j in post-fire years 1, 2, 3, and 5. Data used**

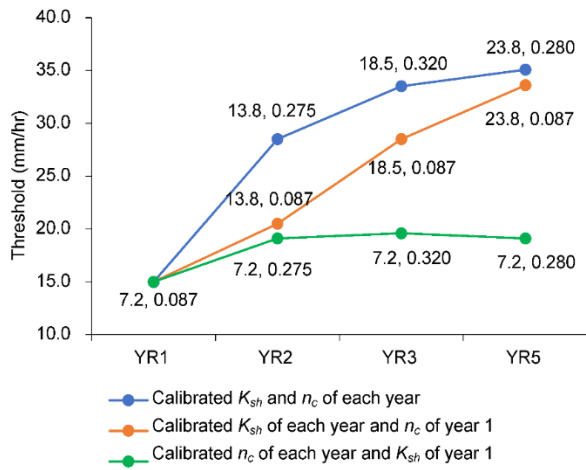
718 **to analyze is from events with peak discharge greater than $2 \text{ m}^3/\text{s}$.**

719

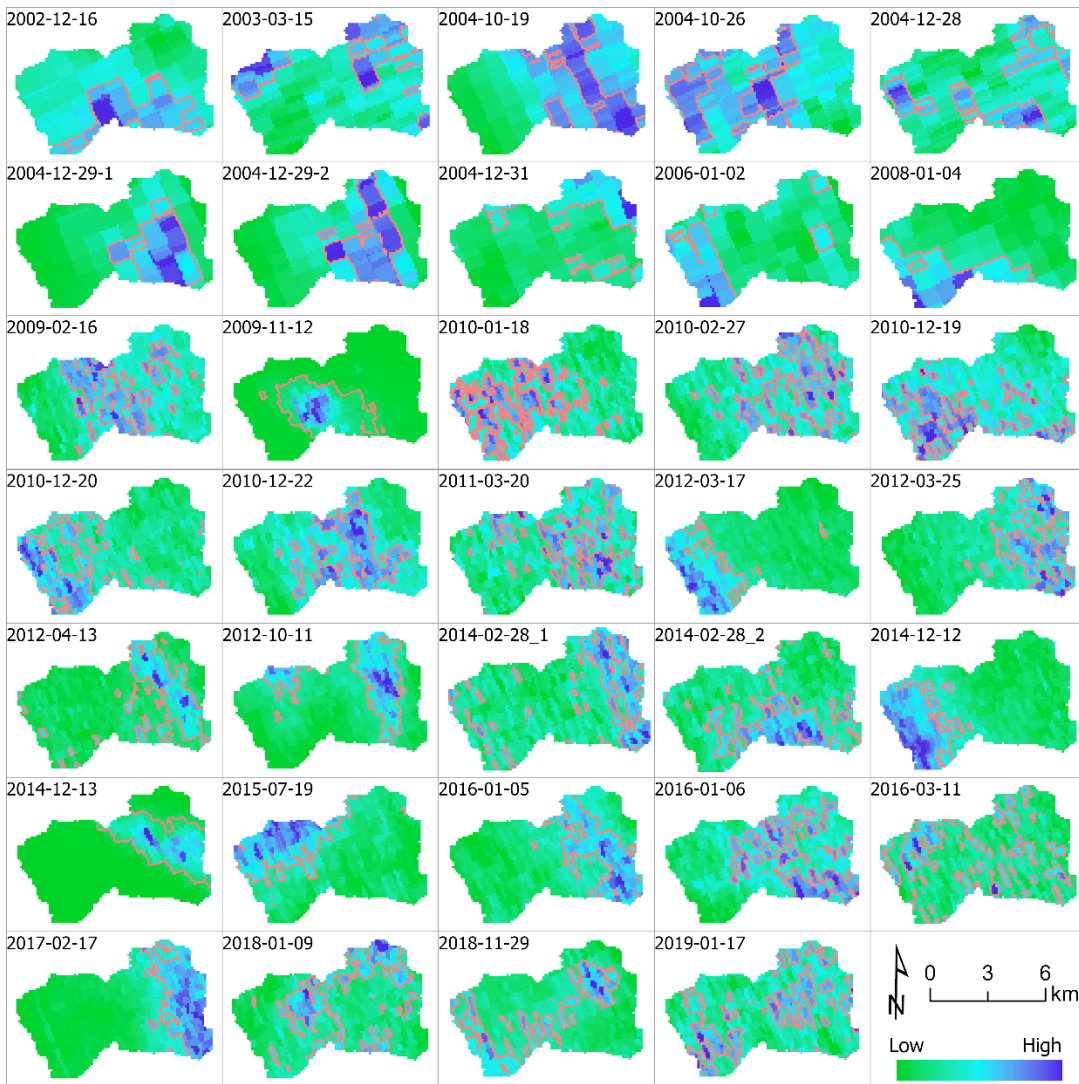


721
 722
 723
 724

Figure 7: The rainfall intensity threshold for flash flood derived from the maximum of TS for different durations and percentiles of the most intensive rainfall field in post-fire years 1, 2, 3, and 5.

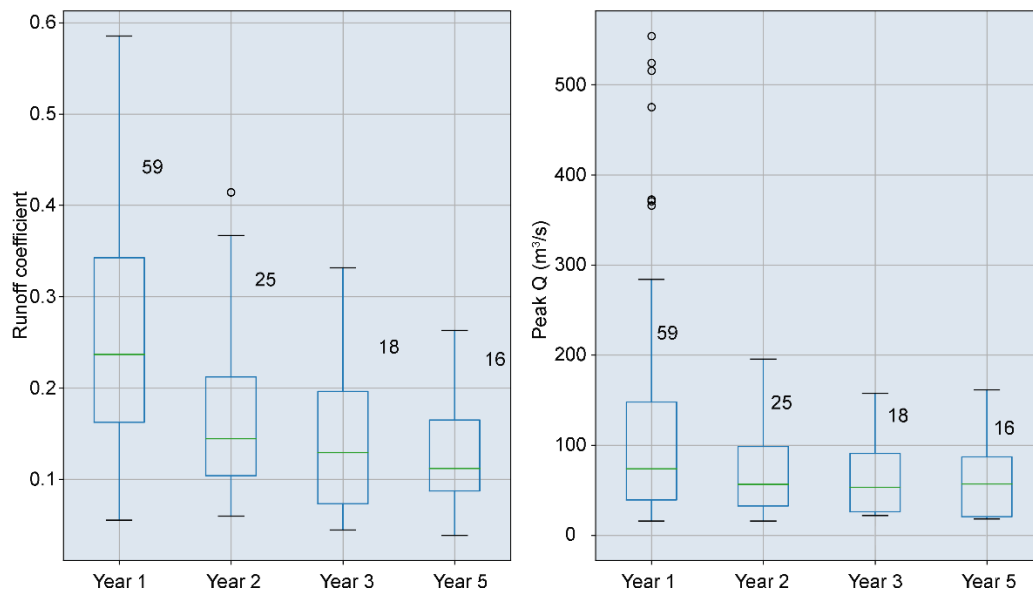


726 **Figure 8: The ROC (receiver operating characteristic) based thresholds for I_{30}^{75} in each year with different model**
 727 **settings. Pairs of K_{sh} (saturated hydraulic conductivity on hillslopes) and n_c (Manning s_n in channels) in each model**
 728 **are along with the data points.**
 729



731 **Figure 9: Snapshots of the spatial patterns of I_{30}^{75} of 34 unique storms. The peak j^{th} percentile of I_D (rainfall intensity**
 732 **over a duration D) is denoted as I_D^j . I_{30}^{75} is the peak value of the 75st percentile of I_{30} (rainfall intensity over 30-min).**
 733 **Red contours delineate the pixels with rainfall intensities larger than I_{30}^{75} of each storm.**

734



736 **Figure 10: Box plots showing the runoff coefficient and peak discharge of flash floods in post-fire year 1, 2, 3, and 5.**
 737 **The numbers of flash floods in each year are displayed next to the box.**
 738